Corrosion Science 131 (2018) 300–309

Contents lists available at ScienceDirect

Corrosion Science

journal homepage: www.elsevier.com/locate/corsci

On the AA2198-T851 alloy microstructure and its correlation with localized corrosion behaviour

Uyime Donatus[a,*], Maysa Terada[b,c], Carlos Ramirez Ospina[c], Fernanda Martins Queiroz[a], Aline Fatima Santos Bugarin[a], Isolda Costa[a]

[a] Instituto de Pesquisas Energéticas e Nucleares, Av. Prof. Lineu Prestes, 2242, São Paulo, Brazil
[b] Escola Politécnica da Universidade de São Paulo, Av. Professor Mello Moraes, 2463, São Paulo, SP, Brazil
[c] Centro Nacional de Pesquisas em Energia e Materiais (CNPEM), Laboratório Nacional de Nanotecnologia (LNNano), Rua Giuseppe MaximoScolfaro 10.000, 13083-100, Campinas, SP, Brazil

ARTICLE INFO

Keywords:
A. aluminium
B. TEM
B. SEM
C. pitting corrosion

ABSTRACT

The corrosion behaviour of AA2198-T851 alloy has been investigated using a combination of immersion tests and different microscopy techniques. Results showed that severe localized corrosion initiated within 1 h of corrosion immersion test in 0.01 mol L^{-1} NaCl solution. The corrosion mechanism in this alloy is intragranular and it propagates crystallographically. The propagation occurs through grain orientation dependent bands and it can be likened to the movement of dislocation through slip planes. Corrosion rings around stable pits result from pH variations. Secondary pits form around primary pits within corrosion rings and are preceded by hydrogen evolution.

1. Introduction

The growing need for materials with high strength and low density for aerospace application has led to a great interest in the Al-Li alloys [1,2]. The modern third generation Al-Cu-Li alloys contain lower Li levels(from 0.9 wt% to 1.1 wt%) in comparison with the Al-Li alloys of the first and second generations which have Cu concentrations in the range from 2.9 wt% and 3.3 wt%. The Al-Cu-Li alloys of third generation are designated as 2XXX series alloys due to their higher Cu content compared with that of Li. They have been developed in an attempt to overcome the shortcomings of the first and second generation Al-Li alloys; for instance, the low short-transverse fracture toughness that might result in unpredictable failures during manufacturing [3,4]. In addition to the distinct advantages of the third generation Al-Li alloys over the first and second generation alloys, Al-Li alloys generally show great benefits for use as structural components in aircrafts, such as density reduction, stiffness increase and fatigue crack growth resistance [5] which has prompted persevering research on the Al-Li alloys in recent times. The weight reduction by Li addition is of major importance for aerostructures. For each 1 wt% Li added to Al, density is reduced by 3% and modulus of elasticity is increased by almost 6% [4–6]. Consequently, the third generation Al-Li alloys have been considered as potential replacements for the AA2024-T3 alloy due to their highly desirable combination of mechanical properties [3,7]. However, reports in the literature has indicated that the Al-Cu-Li alloys are highly susceptible to localized corrosion, mainly characterized by selective attack of certain grains and grain boundaries [8–16].

The investigation on the time dependent evolution of the localized corrosion in the highly important new generation alloys is crucial. In addition to this, identifying and ranking the predominant factors responsible for the corrosion susceptibility of these alloys are also very important. Debates exist in literature on the predominating factors responsible for the types of corrosion attack, intergranular and inter/subgranular, often observed in these alloys. Whilst some authors have strongly associated the corrosion susceptibility of these alloys to grain stored energy (dislocation density per grain), degree of plastic deformation/large Schmid factor values of susceptible grains [8,9,17], others have associated it to the precipitation of T1 (Al_2CuLi) phase at grain/subgrain boundaries and within the grains [6,12–15]. The common ground, however, is that the degree of prior deformation affects the volume of T1 phase preferentially precipitated at grain boundaries, subgrain boundaries and dislocation sites within the grains. It is important to mention that the T1 phase is the major strengthening phase in Al-Cu-Li alloys with Li composition in the range of 0.9 wt% to 1.1 wt% as mentioned earlier. Depending on the composition of the Al-Li alloy and thermomechanical treatment conditions, other precipitation hardening phases such as the δ' (Al_3Li) phase, the Θ'/Θ" (Al_2Cu) phase, and the S (Al_2CuMg) phase can be found [18–20]. It is believed

* Corresponding author.
E-mail address: uyimedonatus@yahoo.com (U. Donatus).

https://doi.org/10.1016/j.corsci.2017.12.001
Received 2 August 2017; Received in revised form 5 December 2017; Accepted 5 December 2017
Available online 08 December 2017
0010-938X/

that the final precipitation state in this alloy is reached via a complex sequence that involves solute clusters, GP zones, δ' and T_1 phases [21].

The T_1 (Al_2CuLi) metastable strengthening phase formation [21,22] is seemingly promoted by Cu and Mg addition at the expense of δ' (Al_3Li) phase. The δ' (Al_3Li) phase forms along the grain boundaries and can be detrimental to intergranular corrosion resistance [23]. On the other hand, it leads to increased strength. This phase is dispersed homogeneously throughout the matrix phase but is not usually found for Li contents below 1.3 wt% [24]. The elimination of the δ' (Al_3Li) phase from an Al-Li alloy is expected to increase the resistance of the alloy to intergranular corrosion. However, amongst all these age-hardening phases, the T1 one has been considered the one of highest metallurgical interest in terms of strengthening and corrosion resistance of the new generation Al-Li alloys.

It is noteworthy to mention that whilst there are numerous reports on the corrosion behaviour of the new generation Al-Li-Cu alloys, reports on the corrosion behavior of AA2198-T851 are scarce. Moreto et al. [7,25] included the AA2198-T851 in their studies where they compared the corrosion resistance of AA2198-T851 with AA2524-T3, however the main focus of their work was not based on showing the corrosion morphology or evolution of corrosion on the surface of the AA2198-T851 alloy over time. Besides, according to those authors, this alloy may present a higher long-time resistance to pitting corrosion when compared with AA2524-T3 base line alloy [25]. From previous studies carried out in our laboratory, the highest susceptibility to localized corrosion was associated to the AA2198-T851 compared with the AA2024-T3 and AA2524-T3 alloys [26]. The conflicting results informed the need for further investigation on this alloy since it is clear that the corrosion behavior of this alloy is far from being fully understood.

In this paper, the localized corrosion resistance of the AA2198-T851 has been investigated by immersion test in 0.01 mol L^{-1} NaCl solution. The evolution of corrosion on the alloy surface was monitored by surface observation as a function of time of immersion using field emission gun – scanning electron microscopy (FEG-SEM). A combination of optical microscopy (OM), scanning electron microscopy (SEM) and transmission electron microscopy (TEM) was used to examine the microstructure in order to correlate it with the corrosion attack morphology.

2. Materials and methods

The chemical composition of the AA2198-T851 used in this study was analysed by optical emission spectroscopy and the result is shown in Table 1. T851 treatment corresponds to solution heat treatment, quenching, stretch relief and artificial aging. The AA2198-T851 was produced by Constellium, France. A commercial grade AA2024-T3 alloy was also used for comparative study.

The samples surface for exposure to the corrosive environment was prepared by successive grinding with silicon carbide papers #800, #1200 and #4000 and then polished with diamond pastes up to 1 µm finish. Following mechanical polishing, samples were degreased in acetone (analytical grade), rinsed in deionized water and dried under a cool air stream. Prior to corrosion immersion tests, microstructural examination was carried out on dried samples using a Leica DMLM coupled microscope, a field emission gun – scanning electron microscopy (FEG-SEM) FEI Quanta 650 equipped with energy dispersive x-ray (EDS) facility and a JEM-2100F transmission electron microscope operating at 200 kV. Scanning transmission electron microscopy (STEM) images were acquired using bright field (BF), annular dark field (ADF) and high angle annular dark field (HAADF) detectors. Samples examined under the microscope for the revelation of grain features were etched in a solution comprising 2% hydrofluoric and 25% nitric acid. Transmission electron microscopy samples were prepared by twin-jet electropolishing using 35% HNO_3 acid in methanol. The solution was maintained at temperatures below −35 °C. The electropolished samples were obtained by preparing a 3 mm disc from samples mechanically ground to less than 100 µm.

Immersion test was conducted for 48 h and samples were removed from the solution for analyses under the FEG-SEM after 3 h, 5 h, 7 h, 9 h, 13 h, 24 h and 48 h. Agar gel corrosion visualization test was conducted by using a viscous liquid prepared by adding 1.5 g of agar powder and 3.75 mL of phenolphthalein in a boiling 3.5 wt.% NaCl solution. Also, immersion tests were conducted in EXCO solution comprising 4 M NaCl, 0.5 KNO_3 and 0.1 M HNO_3 in 1 L deionized water.

3. Results and discussion

3.1. Microstructural characterization

In this section, the observed microstructural features in the AA2198-T851 prior to corrosion tests are presented and discussed.

3.1.1. Grain features and constituent particles

Displayed in Fig. 1(a) and (b) are optical micrographs showing typical grain morphologies and features on the surface and cross section of the alloy. The grains are equiaxed at the surface but when viewed from the cross-section, elongated grains in deformation direction were revealed. Depending on grains orientation, patches of organized parallel striations (and intersecting parallel striations) were observed, as can be seen from darker grains. Features like these have been reported by Donatus and co-workers [27,28] in AA5083-O and AA6082-T6 alloys. In their work, it was shown that these features are in every grain but inclined differently according to grains orientation. It was claimed that these features affect the alloys corrosion mechanisms, and it appears to have an influence on the corrosion propagation mechanism of the alloy investigated in this work, as will be seen later.

Fig. 1(c) shows another feature discernible at low magnification – the constituent particles (coarse intermetallic particles). These particles are aligned as stringers in the mechanical working direction. They are insoluble Fe rich compounds that also contain Cu and Si [29]. Coarsening of these phases during homogenization has been attributed to Mn and Si atoms in the alloys matrix being attracted to these particles [30]. The coarse particles presented in this work do not contain Mn once this element is not present in the alloys. They are majorly Fe and Cu rich intermetallics. It must be mentioned that Mn rich constituent particles stimulate recrystallization [30]. The benefit is that stress free grains (with low dislocation density) tend to promote the formation of coarse T1 phase at the grain boundaries which is detrimental to intergranular corrosion resistance. EDS analyses were conducted on more than 10 particles and the results showed that these particles contain varying Fe:Cu ratios. Some particles showed varying ratios Fe:Cu inside them, with the outer part and inner parts containing different Fe:Cu ratios, in agreement with the reports of Ma and co-workers for AA2099 [31] With regard to corrosion, constituent particles or coarse intermetallic particles cause trenching of the surrounding aluminium matrix leading to observable cavities on the surface of the alloy. In this work,

Table 1
Chemical composition (wt%) of the AA2198-T851 alloy studied.

Elements	Cu	Mg	Si	Mn	Fe	Zn	Li	Ti	Zr	Ag	Al
Weight%	3.68	0.31	0.03	–	0.08	0.01	1.01	0.027	0.12	–	Balance

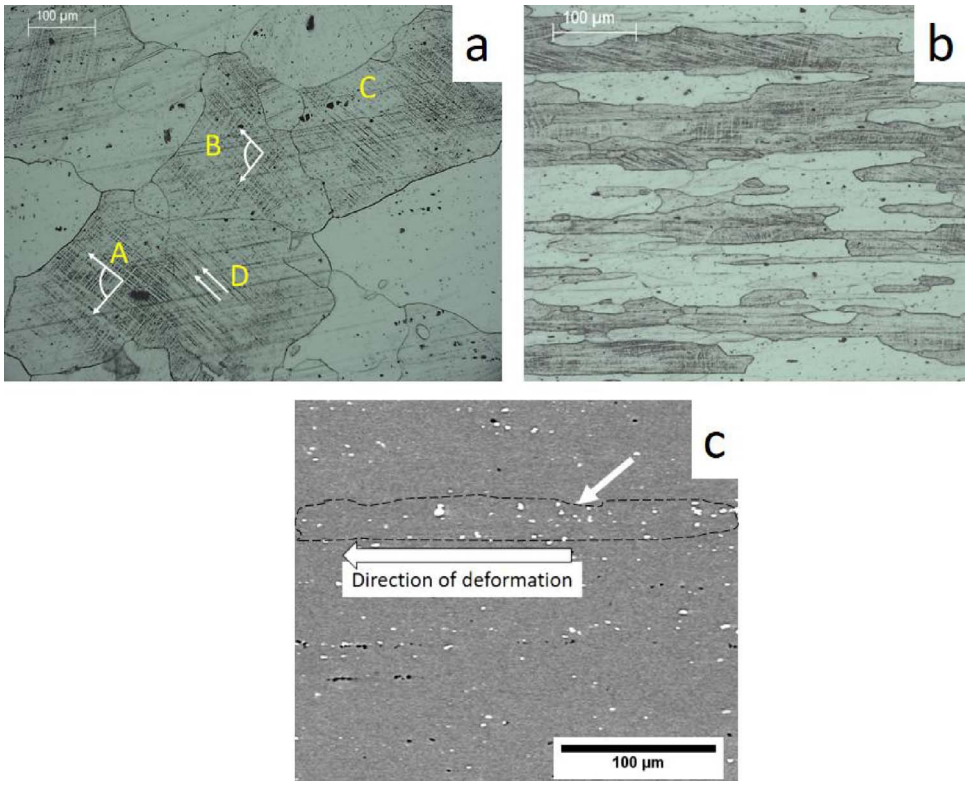

Fig. 1. (a) Plan view and (b) cross sectional optical micrographs displaying grain dependent striations in certain grains. (c) Scanning electron micrographs displaying stringers of constituent particles in the direction of deformation.

similar features were observed overtime. This is discussed in Section 3.2. There was no evidence to suggest that they cause severe localized corrosion over time.

3.1.2. Dispersoids and strengthening phases

Dispersoids are nano to micron range sized second phase particles that significantly have effect on recrystallization, grain growth and grain size control. There are basically three types of dispersoids present in aluminium alloys: the Al_6Mn, the $Al_{20}Cu_2Mn_3$ and the Al_3Zr phases [4]. In the investigated alloy, only the spherical Al_3Zr dispersoids are present. A typical Al_3Zr dispersoid is shown in Fig. 2(a) with diameter in the range of approximately 20 nm. The Al_3Zr (and other dispersoids) forms during homogenization by forming a metastable $L1_2$ Al_3Zr which later transforms to the stable DO_{23} Al_3Zr phase after prolong heating [22,30,32]. Apart from works like the work of Ma [11] where the differential oxidizing effects of the $Al_{20}Cu_2Mn_3$ and the Al_3Zr dispersoids have been related to the anodizing response of the AA2099 aluminium alloy, and the works of Birbilis and Buchheit [33] where the corrosion potentials of the dispersoid compositions was investigated, there are no clear evidences relating dispersoids to localized corrosion of Al alloys. However, the Al_3Zr dispersoid in particular, does affect recrystallization and this in turn can influence dislocation density and the precipitation of T1 phase which significantly influences the localized corrosion response of the alloy. Thus, controlling the homogeneous distribution of the Al_3Zr dispersoid is important, but this has been a major challenge [30,32] and this is reflected in this alloy; the presence of the significantly varied grain sizes and or uneven formation of subgrains can be attributed to this.

As stated earlier, the T1 phase is the phase of highest metallurgical interest in new generation Al-Cu-Li alloys as it majorly dictates the strength level of the alloy and, debatably, the localized corrosion resistance of the alloy. The TEM micrographs displayed in Fig. 2(b) show the predominance of the T1 phase in the structure of the alloy. The analysis of the selected FFT along [101] zone axis and the simulation of the HRTEM images in Fig. 3(a) and (c) confirm the presence of T1 phase. The T1 phase has a hexagonal platelet structure and lies on the

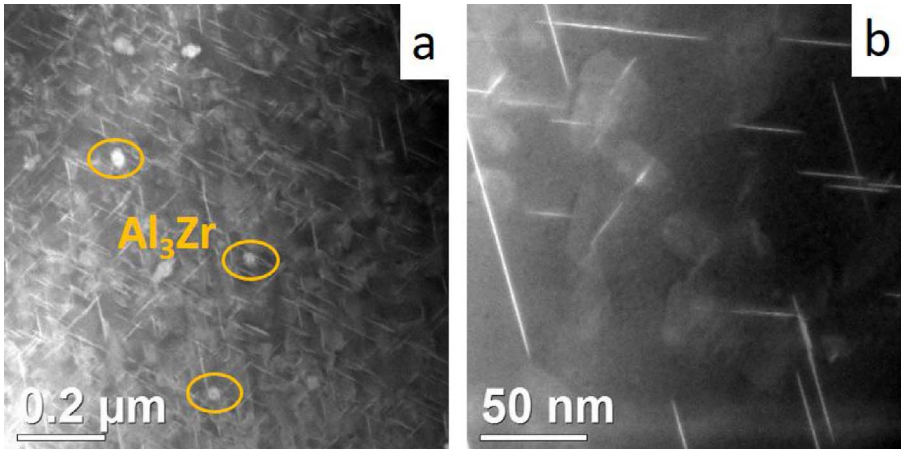

Fig. 2. TEM images of AA2198-T851 aluminium alloy. (a) ADF image showing the Al_3Zr dispersoid and other nano-sized precipitates. (b) HAADF image showing the T1 phase.

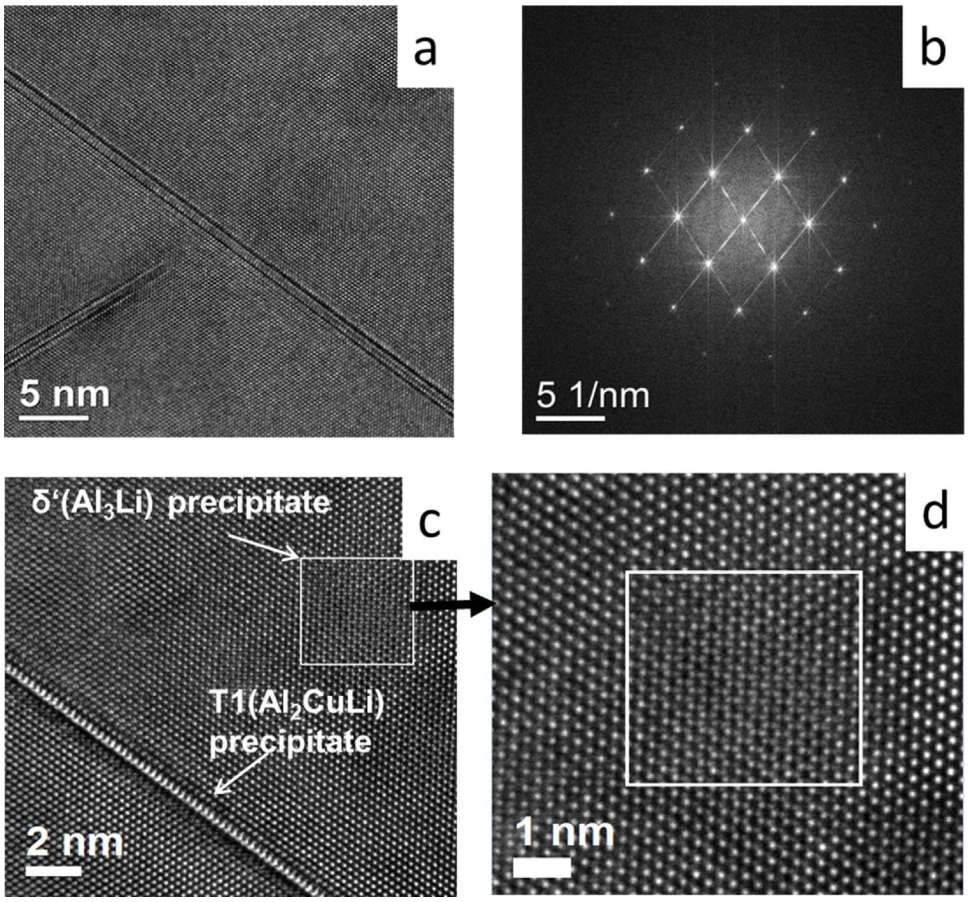

Fig. 3. (a) HRTEM image of the T1; (b) FFT along [101] zone axis; (c) Higher HRTEM image of (a); and (d) Enlarged HRTEM image of the δ' phase.

{111} habit planes, with $[0001]_{T1}//[111]_{\alpha}$, $[1010]_{T1}//[110]_{\alpha}$ orientation relationship with the matrix, space group of *P6/mmm* with lattice constants a = 0.4964 and c = 0.9345 [19,22,31]. The analysis also confirmed the presence of highly coherent δ' (Al_3Li) phase (Fig. 3(d)); however, the δ' (Al_3Li) were not in any way dominant and were rarely found in this alloy. The T1 phase is the predominant strengthening phase as it is very efficient at blocking slips [34,35]. In spite of the beneficial effect of the T1 phase on the mechanical properties of the Al-Cu-Li alloys, its effect on the corrosion resistance remains controversial. The literature reports that it might either undergo selective dissolution along with the dissolution of the adjacent Al matrix forming large pits or dissolve near to the precipitate free zone forming small pits [6,16,36]. In this case, localized corrosion in the form of intragranular corrosion might also be associated with this phase (this is further discussed in Section 3.2.)

3.2. Corrosion morphology and mechanism

This section presents the observed microstructural evolution in the AA2198-T851 alloy during different corrosion tests. Figs. 4–7 show the secondary electron micrographs of the AA2198-T851 surface after varying periods of exposure to naturally aerated 0.01 mol L^{-1} NaCl solution at 22 ± 1 °C exhibiting the evolution of corrosion on the alloy surface. On immersion, severe localized corrosion (SLC) initiated within the 1st hour. The areas associated with the initiated pits increased continuously after initiation until about 36 h, and no further increase in the widths of the pits was observed afterwards since the SLC sites were covered with voluminous corrosion products (Figs. 6 and 7). On the average, the widths of the pits were in the range of: 30–70 μm after 7 h; around 40–85 μm after 9 h; 100–200 μm after 13 h; and 200–400 μm after 24 h. The increasingly active areas exposed to the electrolyte were due to the action of a combination of low pH and the presence of higher concentration of chloride ions at the active corrosion front compared with the rest of the matrix. This lead to local depassivation at the active corrosion front with subsequent exposure of new surface area to the anolyte solution.

In addition to increasing severe localized corrosion areas, other notable microstructural features observed on the surface of the alloy after immersion tests were: (i) cavities and trenches around cathodic intermetallic particles (Fig. 4); (ii) stable pitting sites with protected circular regions (Fig. 5 (a) and (b)); (iii) grain orientation dependent crystallographic corrosion (Fig. 5(c) and (d) and Fig. 6); (iv) intergranular corrosion (Fig. 7(a)); and (v) voluminous corrosion products (Fig. 7(b)–(d)).

The trenches observed around cathodic intermetallic particles (indicated with black arrows in Fig. 4) resulted from the dissolution of the surrounding anodic aluminium matrix which has a lower potential compared with the Fe and Cu rich coarse intermetallic particles. The localized cavities mostly resulted from detachment of constituent particles with dimensions up to 8 μm in diameter, after the dissolution of the aluminium matrix surrounding these particles. Distribution of cavities and trenches (indicated with white arrows) were dependent on constituent particles distribution in the alloy, which are mostly aligned in the deformation direction. These cavities and trenches around cathodic coarse particles are common in aluminium alloys and has also been reported for the AA2099-T83 Al-Cu-Li alloy recently [8].

The form of severe localized corrosion (SLC) observed in this alloy is majorly intragranular. It occurs in the form of a central pit with a circle-like region corresponding to a protected area within which corrosion products or activities are hardly found (see the white arrow in Fig. 5(a) and (b)). This type of localized corrosion has been reported in literature for the AA2099-T83 alloy [37] and was associated with the surface regions where gas evolution was observed during immersion. The evaluation of the corroded surface through microscopy reveal that once

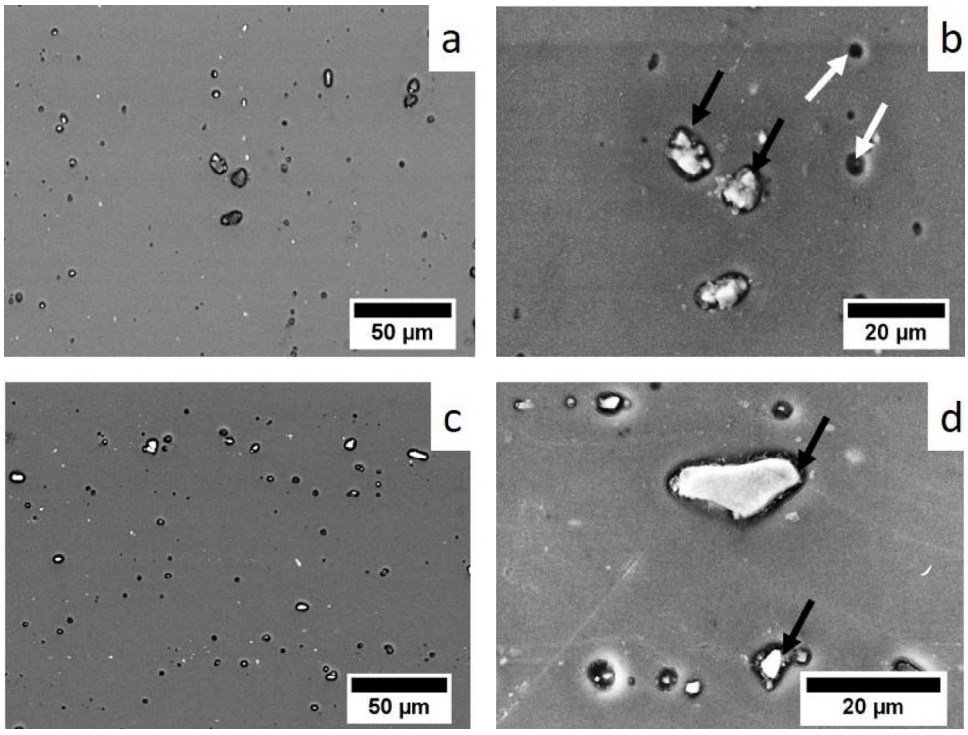

Fig. 4. AA2198-T851 alloy surface after up 3–5 h exposure to 0.01 mol L^{-1}NaCl solution showing cavities and trenches around cathodic intermetallics.

corrosion is initiated, the active site acts like a sacrificial anode, cathodically protecting a circular area within its vicinity. Selected images of agar gel corrosion visualization studies presented in Fig. 8 reveal more about this circular area within the vicinity of the SLC region. The images in Fig. 8(a)–(c) were obtained after 24, 48 and 78 h respectively, and the image in Fig. 8(d) was obtained after the removal of the agar gel. In Fig. 8(a)–(c), pink coloration indicates the predominance of hydroxyl ions, while colourless coloration indicates the predominance of hydrogen ions. The hydroxyl ions result from the cathodic reduction of O_2 ($O_2 + 2H_2O + 4e^- \rightarrow 4\,OH^-$). For the production of hydrogen ions, first there is the anodic dissolution of Al to produce Al^{3+} ($Al \rightarrow Al^{3+} + 3e^-$), then there is the hydrolyses reaction to produce the H^+ ions ($Al^{3+} + 3H_2O \rightarrow Al(OH)_3 + 3H^+$). The images in Fig. 8 actually reveal that the pH in the supposed protected area is low, and this aids

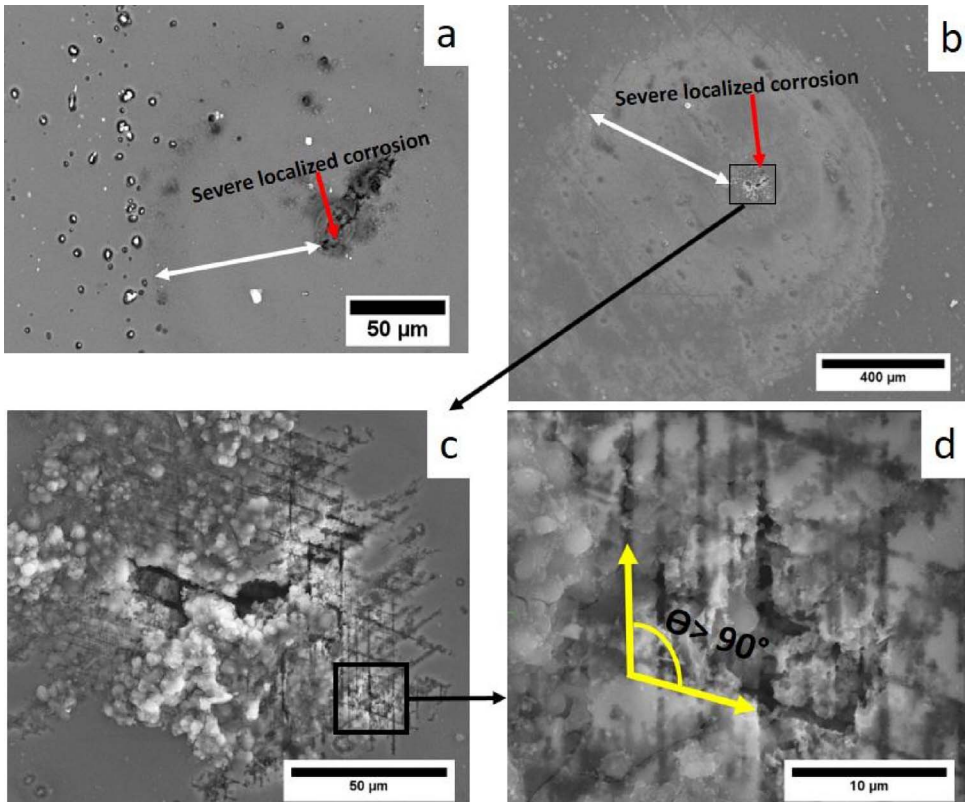

Fig. 5. AA2198-T851 alloy surface after (a) 7 and (b)–(d) 9 h exposure to 0.01 mol L^{-1}NaCl solution showing stable pitting sites.

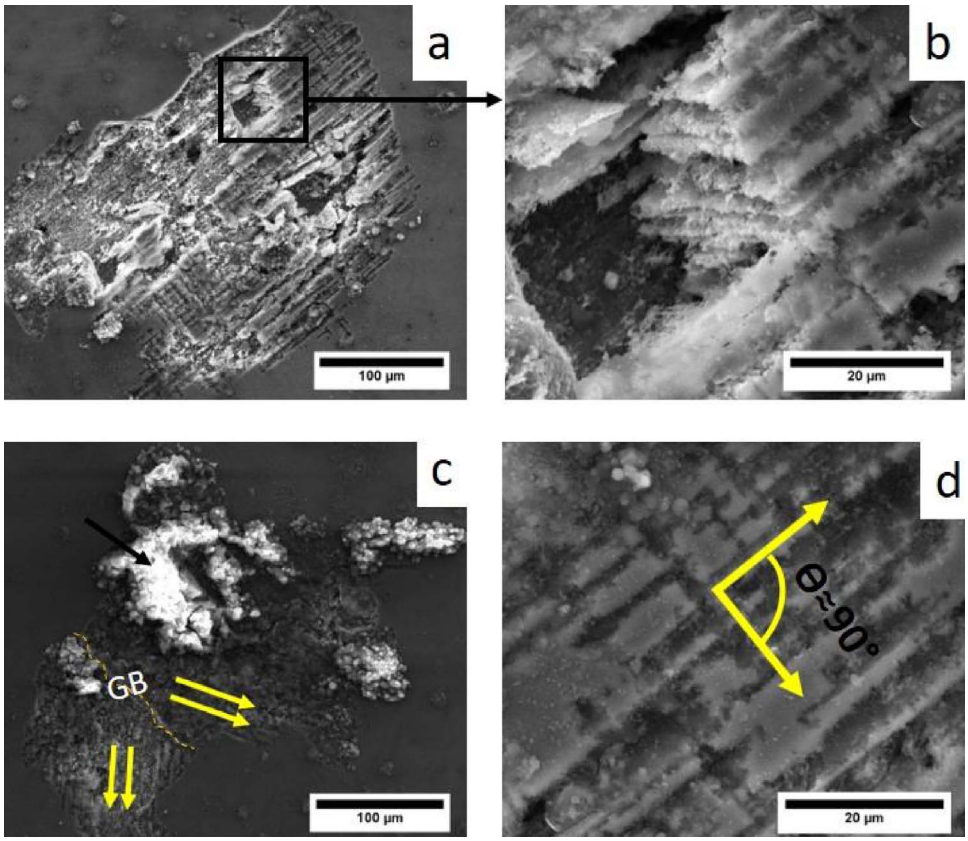

Fig. 6. AA2198-T851 alloy surface after 13 h exposure to 0.01 mol L^{-1}NaCl solution showing pits with increased widths and crystallographic corrosion morphology.

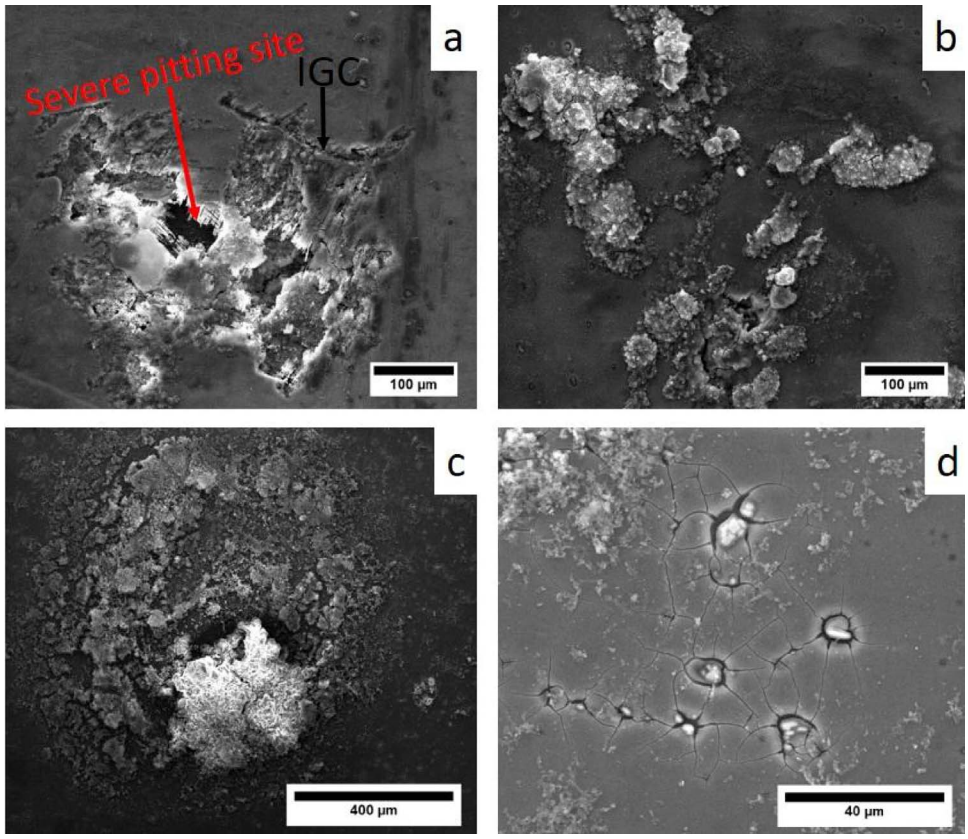

Fig. 7. AA2198-T851 alloy surface ((a) and (b)) after 24 h and ((c) and (d)) after 48 h of exposure to 0.01 mol L^{-1} NaCl solution.

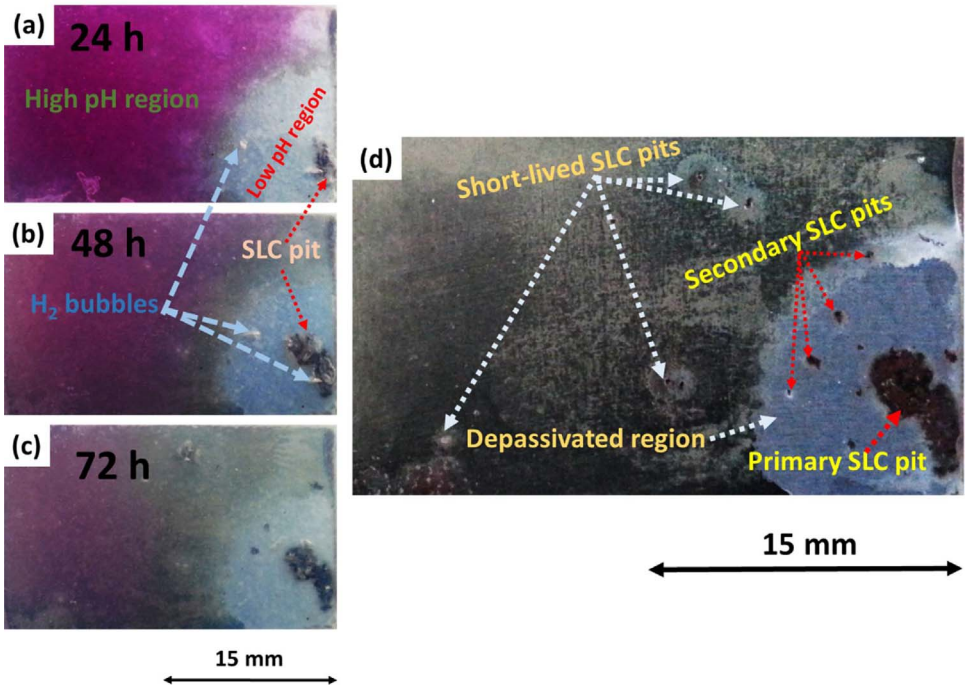

Fig. 8. Optical images of agar gel corrosion visualization test of the AA2198-T851 after (a) 24, (b) 48 h, (c) 72 h and (d) the removal of the agar gel.

the growth of the SLC pit. As earlier mentioned, the local pH reduction, in combination with the presence of higher chloride concentration causes local depassivation at the corrosion front which leads to the exposure of new surface area to the anolyte solution. Additionally, it is also clear that the bulk cathodic reduction of oxygen that results in the production of hydroxyl ions occurs at multiples of mirometers away from the actual stable pitting site (depending on the intensity of the attack); about 10 mm radially in this case. The apparent radial pH demarcation, thus, reveal that the often observed corrosion rings [38] on the corroded surfaces of Al alloys are often due to the difference in pH between the vicinity of the stable pitting sites and the surrounding regions where the cathodic reduction of O_2 occurs. In many cases, increased volume of lumps of corrosion products are often observed at the corrosion ring boundary. These additional corrosion products are predominantly salts that most likely resulted from the interaction between the low pH solution (within the ring) and the higher pH solution (outside the ring).

Further, it was interesting to note that hydrogen bubbles, different from the one occurring at the corrosion front of the primary SLC pit, started to evolve at the near edges of the rings after about 24 h. These bubbles preceded the occurrence of secondary SLC pits (as indicated in Fig. 8(d)) that formed around the primary SLC pit. The manner of appearance of the secondary SLC pits suggests that they are from the subsurface propagation/spread of the primary SLC pit. The same phenomena was also observed in other tested samples. It is also important to mention that over six SLC sites were initiated at the early hours of the corrosion test, and these sites were clearly observable after about 4 h. However, only one of the SLC pit (the primary SLC pit) thrived. The others were short-lived, and their depassivated corrosion ring regions became repassivated over time with the eventual occurrence of cathodic reduction reactions in such regions. This is evident from the pink coloration that later covered these regions.

With respect to the corrosion propagation mechanism, a closer observation of the AA2198-T51 sample exposed to the 0.01 mol L^{-1} NaCl solution at higher magnifications (Fig. 5(c)–(d)) revealed a crystallographic corrosion morphology. After pit initiation, propagation occurred mostly along the boundaries of series of parallel and intersecting striations. These striations are grain orientation dependent and their inclinations and angles of intersection differ from grain to grain. This is clearer when corrosion pathways [39] in the grains shown in Figs. (d), (c) and (d) are compared. As an example, the striations observed in Fig. 5(d) intersects at an obtuse angle whilst those in Fig. 6(d) intersects at about 90°, and those in Fig. 6(c) are parallel. Similar features were revealed in the grains of AA5083-O and AA6082-T6 alloys [27,28] and these striations were suggested to be related to {100} planes that are also the habit planes of the strengthening Mg_2Si phase in the AA6082-T6 alloy. In this work, the susceptibility and inclinations of the striations suggest that these are aligned parallel to {111} planes which are the habit planes of T1 phase. Proton and co-workers [14] also observed similar features; they appeared as parallel bands in welded AA2050. They attributed the corrosion attack to T1 phase distribution. It must be mentioned that the T1 phase is the major cause of the high corrosion susceptibility of the new Al-Cu-Li alloys generation.

For further understanding of the corrosion morphology and mechanism of the alloy, and to find out whether a decrease in pH of the electrolyte could revert the corrosion behavior, corrosion immersion test was conducted in EXCO solution. The results from the AA2198-851 alloy were compared with that from the conventional AA2024-T3 aluminium alloy. Presented in Fig. 9 are the optical micrographs of the surfaces of the AA2198-T851 and AA2024-T3 alloys after 2 h of exposure to the EXCO solution. Again, the AA2198-T851 alloy only shows intragranular corrosion with pathways associated with the grain orientation dependent bands. No form of intergranular corrosion was observed; in fact, the grain boundaries were intact (as indicated by the blue arrows). This is interesting as the EXCO specifically attacks more of grain boundaries in other Al alloys. Another important observation was that corrosion products and hydrogen bubbles (as indicated by the red arrows) were observed to be coming out of the attack front despite the fact that the sample had been thoroughly rinsed and air dried for hours prior to the examination. In contrast, on the AA2024-T3 alloy, which was clearly far less susceptible to corrosion, it was difficult to find corrosion products and hydrogen bubbles coming out of the attack front. And for the AA2024-T3 alloy, the attack was mainly intergranular and was far less severe compared with that of the AA2198-T851 alloy.

The cross-sectional micrographs of the AA2198-T851 alloy exposed to 24 h of test, presented in Fig. 10, also clearly shows that the grain boundaries in this alloy are more noble compared with the grain interior. What this implies is that, the T1 phase is not in abundance at the

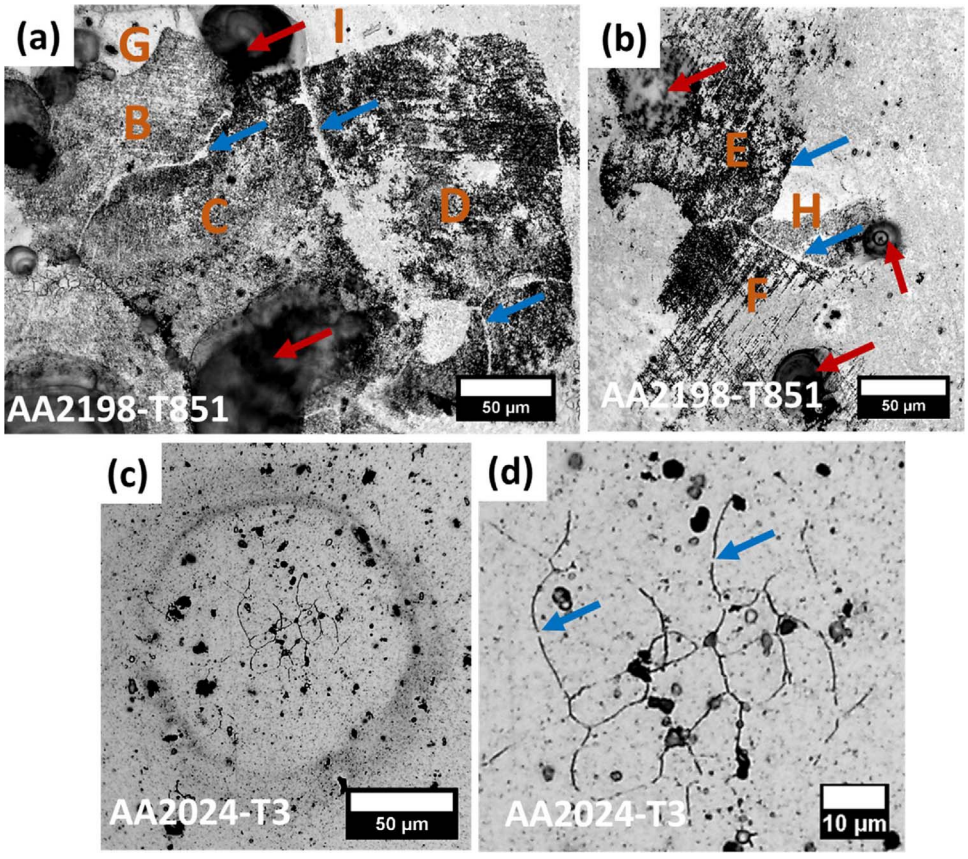

Fig. 9. Optical images of the surfaces ((a)-(b)) AA2198-T851 alloy and ((c)-(d)) AA2024-T3 alloy after 2 h immersion test in EXCO solution.

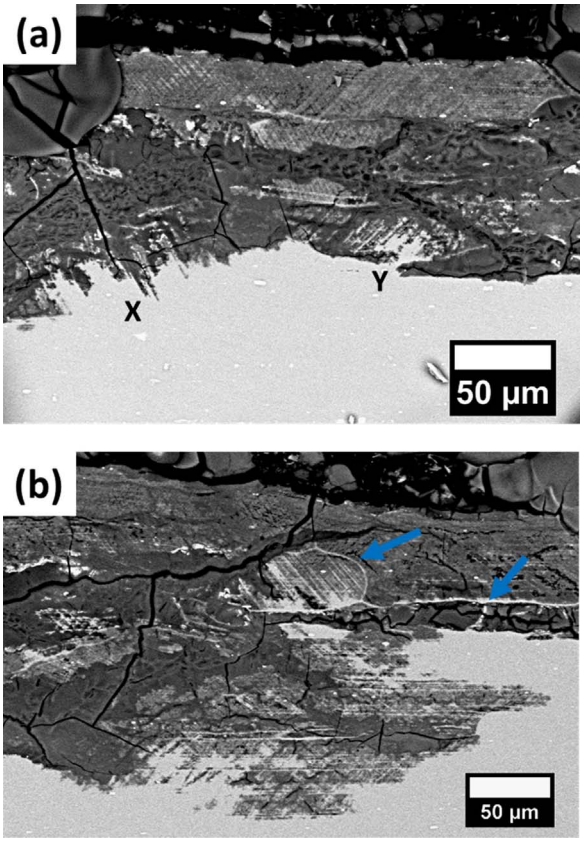

Fig. 10. Optical images of the cross-section of the AA2198-T851 alloy after 24 h immersion test in EXCO solution.

grain boundaries of this alloy, if present at all. In addition, the grain orientation dependent propagation pathways beneath the near surface of the alloy is also evident as indicated by X and Y in Fig. 10(a).

The corrosion propagation mechanism in this alloy can be compared to that of slip mechanism during deformation. A schematic diagram is presented in Fig. 11 to illustrate this. The AA2198-T851 alloy contains parallel bands or alternate layers that are grain orientation dependent, as represented in grains A, C, D, and E. The micrograph in Fig. 6(b) also clearly shows this. Similar features observed in the AA5083-O and AA6082-T6 alloys, in a reported work [27], were referred to as grain distinct nanolayers and their dimensions were argued to be dependent on the thermo-mechanical history of the alloys. The layers in grains B and F are assumed to be exposed at inclinations normal to the exposed surface. These parallel bands consist of active and more noble regions alternately, and this is in agreement with published works [27,28,39]. In this case, the active regions most likely contain higher volume fraction of T1 phase compared with the other regions, and it is the interspace between the more noble layers in the grains. After the initiation of corrosion, the attack propagates through the active interspace at a faster rate, and in a direction that is dependent on the corrosion pathway of the grain similar to how dislocation moves through specific slip planes and directions. Subsequently, the attack spreads into the more noble layer but with a slower propagation rate. It should be recalled that a moving dislocation encounters a barrier at the grain boundary (GB) between the previous grain and the new grain (with a different orientation) because the slip system of the new grain does not align with the slip system of the previous grain. The same can be said of the propagating crystallographic attack through the grains of the AA2198-T851 alloy because the propagation pathway is different from grain to grain. A barrier to propagation is encountered at the grain boundary. Eventually, intergranular corrosion may occur, as exemplified in Fig. 7(a), as the corrosion finds its way through the new grain. But generally, the grain boundaries in this alloy are rarely

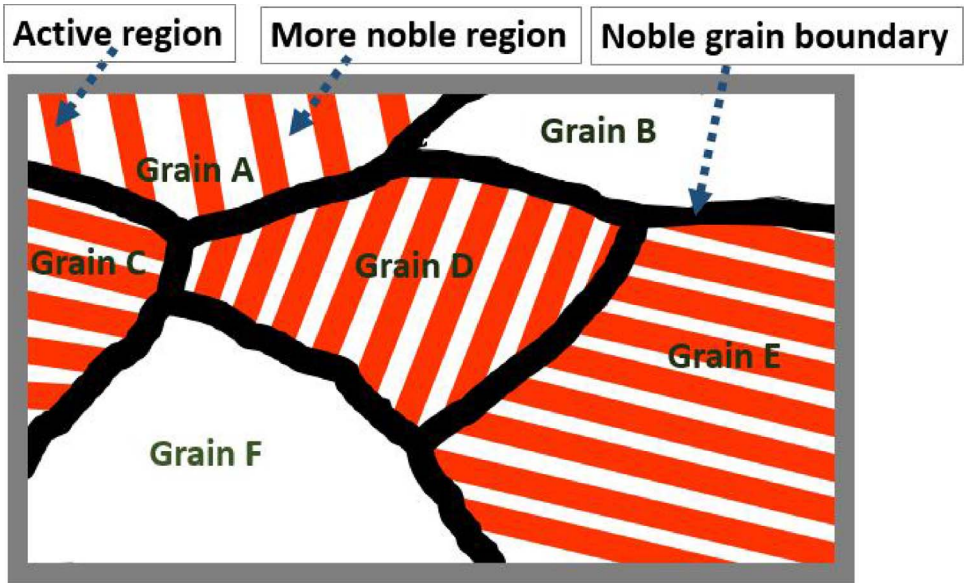

Fig. 11. Schematic diagram showing the grain distinct active bands for corrosion propagation pathways in the AA2198-T851 alloy.

susceptible and the propagation of corrosion is mostly through the grains.

4. Conclusions

1. AA2198-T851 undergoes severe localized corrosion in naturally aerated 0.01 mol L^{-1} NaCl solution within the early hours of immersion in the electrolyte. Pitting mostly occurred within the grain, and when it is initiated it cathodically protects the surrounding regions radially in a ring-like manner.
2. The corrosion rings form due to pH difference between the low pH region of the severe localized corrosion and the high pH regions were cathodic reduction of oxygen occur. Increased lumps of corrosion products form at the corrosion ring boundary due to the interaction between the low pH and high pH solutions.
3. After prolonged hours of severe localized corrosion, secondary pits resulting from the sub-surface spread of the primary pit form around the primary pit, and their occurrence is preceded by the evolution of hydrogen bubbles.
4. The propagation of the corrosion was crystallographic along parallel and intersecting striations aligned parallel to the {111} planes which is the habit planes of the active T1 (Al_2CuLi) phase. T1 phase is associated with localized corrosion susceptibility of this alloy. Increment in immersion times resulted in increased widths of the initiated pits up to about 36 h when no increase in pitting widths were easy to observe due to the formation of voluminous corrosion products afterwards.
5. The corrosion propagation mechanism through specific grain distinct bands in the AA2198-T851 alloy can be likened to the case of slip mechanism through specific slip systems.

Acknowledgements

The authors acknowledge CAPES for financial support to Dr Maysa Terada (Proc. 1536157), FAPESP (Proc. 2013/13235-6 and Proc. 2017/03095-3), CAPES(Capes/Cofecub 806-14), LNNano for TEM analysis and the technical contribution of Joao Victor de Sousa Araujo.

References

[1] P. Cavaliere, M. Cabibbo, F. Panella, A. Squillace, 2198 Al–Li plates joined by friction stir welding: mechanical and microstructural behavior, Mater. Des. 30 (2009) 3622–3631, http://dx.doi.org/10.1016/j.matdes.2009.02.021.
[2] O. Hatamleh, M. Hill, S. Forth, D. Garcia, Fatigue crack growth performance of peened friction stirwelded 2195 aluminum alloy joints at elevated and cryogenic temperatures, Mater. Sci. Eng. A 519 (2009) 61–69, http://dx.doi.org/10.1016/j.msea.2009.04.049.
[3] T. Warner, Recently-developed aluminium solutions for aerospace applictions, Mater. Sci. Forum 519–521 (2006) 1271–1278, http://dx.doi.org/10.4028/www.scientific.net/MSF.519-521.
[4] R.J. Rioja, J. Liu, The evolution of Al-Li base products for aerospace and space applications, Metall. Mater. Trans. A 43 (2012) 3325–3337, http://dx.doi.org/10.1007/s11661-012-1155-z.
[5] N.E. Prasad, A.A. Gokhale, P.R. Rao, Mechanical behaviour of aluminium-lithium alloys, Sadhana 28 (2003) 209–246, http://dx.doi.org/10.1007/BF02717134.
[6] R.G. Buchheit, J.P. Moran, G.E. Stoner, Electrochemical behavior of the T1 (Al2CuLi) intermetallic compound and its role in localized corrosion of Al-2%Li-3%Cu alloys, Corrosion 50 (1994) 120–130, http://dx.doi.org/10.5006/1.3293500.
[7] J.A. Moreto, O.C. Gamboni, C.E.B. Marino, W. Bose Filho, J.C.S. Fernandes, L.A. Rocha, Corrosion behaviour of Al and Al-Li alloys used as aircraft materials, Corros. Prot. Mater. 31 (2012) http://www.scielo.mec.pt/pdf/cpm/v31n3-4/v31n3-4a01.pdf (Accessed 20 July 2017).
[8] Y. Ma, X. Zhou, Y. Liao, Y. Yi, H. Wu, Z. Wang, W. Huang, Localised corrosion in AA 2099-T83 aluminium-lithium alloy: the role of grain orientation, Corros. Sci. 107 (2015) 41–48, http://dx.doi.org/10.1016/j.corsci.2016.02.018.
[9] Y. Ma, X. Zhou, W. Huang, Y. Liao, X. Chen, X. Zhang, G.E. Thompson, Crystallographic defects induced localised corrosion in AA2099-T8 aluminium alloy, Corros. Eng. Sci. Technol. 50 (2015) 420–424, http://dx.doi.org/10.1179/1743278214Y.0000000237.
[10] X. Zhang, X. Zhou, T. Hashimoto, J. Lindsay, O. Ciuca, C. Luo, Z. Sun, X. Zhang, Z. Tang, The influence of grain structure on the corrosion behaviour of 2A97-T3 Al-Cu-Li alloy, Eval. Progr. Plann. (2016), http://dx.doi.org/10.1016/j.corsci.2016.12.005.
[11] Y. Ma, Effect of Microstructure on Corrosion Resistance and Anodising Behaviour of AA 2099-T8 Aluminium Alloy, University of Manchester, 2010.
[12] R.G. Buchheit, J.P. Moran, G.E. Stoner, Localized corrosion behavior of alloy 2090 – the role of microstructural heterogeneity, Corrosion 46 (1990) 610–617, http://dx.doi.org/10.5006/1.3585156.
[13] V. Proton, J. Alexis, E. Andrieu, J. Delfosse, A. Deschamps, F. De Geuser, M.C. Lafont, C. Blanc, The influence of artificial ageing on the corrosion behaviour ofa 2050 aluminium-copper-lithium alloy, Corros. Sci. 80 (2014) 494–502, http://dx.doi.org/10.1016/j.corsci.2013.11.060.
[14] V. Proton, J. Alexis, E. Andrieu, J. Delfosse, M.-C. Lafont, C. Blanc, Characterisation and understanding of the corrosion behaviour of the nugget in a 2050 aluminium alloy friction stir welding joint, Corros. Sci. 73 (2013) 130–142, http://dx.doi.org/10.1016/j.corsci.2013.04.001.
[15] V. Proton, J. Alexis, E. Andrieu, C. Blanc, J. Delfosse, L. Lacroix, G. Odemer, Influence of post-welding heat treatment on the corrosion behavior of a 2050-T3 aluminum-copper-lithium alloy friction stir welding joint, J. Electrochem. Soc. 158 (2011) C139–C147, http://dx.doi.org/10.1149/1.3562206.
[16] C. Luo, S.P. Albu, X. Zhou, Z. Sun, X. Zhang, Z. Tang, G.E. Thompson, Continuous and discontinuous localized corrosion of a 2xxx aluminium-copper-lithium alloy in sodium chloride solution, J. Alloys Compd. 658 (2016) 61–70, http://dx.doi.org/10.1016/j.jallcom.2015.10.185.
[17] X. Zhang, X. Zhou, T. Hashimoto, J. Lindsay, O. Ciuca, C. Luo, Z. Sun, X. Zhang, Z. Tang, The influence of grain structure on the corrosion behaviour of 2A97-T3 Al-Cu-Li alloy, Corros. Sci. 116 (2017) 14–21, http://dx.doi.org/10.1016/j.corsci.2016.12.005.
[18] S.C. Wang, M.J. Starink, Precipitates and intermetallic phases in precipitation hardening Al-Cu-Mgk(Li) based alloys, Int. Mater. Rev. 50 (2005) 193–215, http://

dx.doi.org/10.1179/174328005X14357.
[19] R. Yoshimura, T.J. Konno, E. Abe, K. Hiraga, Transmission electron microscopy study of the evolution of precipitates in aged Al–Li–Cu alloys: the θ′ and T1 phases, Acta Mater. 51 (2003) 4251–4266, http://dx.doi.org/10.1016/S1359-6454(03)00253-2.
[20] R. Yoshimura, T.J. Konno, E. Abe, K. Hiraga, Transmission electron microscopy study of the early stage of precipitates in aged Al–Li–Cu alloys, Acta Mater. 51 (2003) 2891–2903, http://dx.doi.org/10.1016/S1359-6454(03)00104-6.
[21] S.P. Ringer, K. Hono, Microstructural evolution and age hardening in aluminium alloys: atom probe field-ion microscopy and transmission electron microscopy studies, Mater. Charact. 44 (2000) 101–131.
[22] S.C. Wang, M.J. Starink, Precipitates and intermetallic phases in precipitation hardening Al–Cu–Mg–(Li) based alloys, Int. Mater Rev. 50 (2005) 193–215, http://dx.doi.org/10.1179/174328005X14357.
[23] W.N. Garrard, Corrosion behavior of aluminum-lithium alloys, Corrosion 50 (1994) 215–225, http://dx.doi.org/10.5006/1.3293513.
[24] S.Y. Betsofen, V.V. Antipov, I.A. Grushin, M.I. Knyazev, L.B. Khokhlatova, A.A. Alekseev, Effect of the composition of Al-Li alloys on the quantitative relation between the δ′(Al3Li), S1(Al2MgLi), and T1(Al2CuLi) phases, Russ. Metall. 2015 (2015) 51–58, http://dx.doi.org/10.1134/S0036029515010024.
[25] J.A. Moreto, C.E.B. Marino, W.W. Bose, L.A. Filho, J.C.S. Rocha, S.V.E.T. Fernandes, SKP and EIS study of the corrosion behaviour of high strength Al and Al–Li alloys used in aircraft fabrication, Corros. Sci. 84 (2014) 30–41, http://dx.doi.org/10.1016/j.corsci.2014.03.001.
[26] A.F.S. Santos, S. Zacarelli, M. Terada, I. Costa, Effect of microstructure on the corrosion resistance of AA2524-T3 and AA2198 T-851 aluminum alloys used in the aeronautic industry, Eur. Corros. Congr. 82 (2014) 82–97.
[27] U. Donatus, G.E. Thompson, X. Zhou, J. Alias, I.-L. Tsai, Grain distinct stratified nanolayers in aluminium alloys, Mater. Chem. Phys. 188 (2017) 109–114, http://dx.doi.org/10.1016/j.matchemphys.2016.12.021.
[28] U. Donatus, G.E. Thompson, D. Elabar, T. Hashimoto, S. Morsch, Features in aluminium alloy grains and their effects on anodizing and corrosion, Surf. Coat. Technol. 277 (2015) 91–98, http://dx.doi.org/10.1016/j.surfcoat.2015.07.034.
[29] I.J. Polmear, Physical metallurgy of aluminium alloys, Light Alloy, Fourth ed., Elsevier Ltd., 2005, pp. 29–96.
[30] Z. Jia, G. Hu, B. Forbord, J.K. Solberg, Effect of homogenization and alloying elements on recrystallization resistance of Al-Zr-Mn alloys, Mater. Sci. Eng. A. 444 (2007) 284–290, http://dx.doi.org/10.1016/j.msea.2006.08.097.
[31] Y. Ma, X. Zhou, G.E. Thompson, T. Hashimoto, P. Thomson, M. Fowles, Distribution of intermetallics in an AA 2099-T8 aluminium alloy extrusion, Mater. Chem. Phys. 126 (2011) 46–53, http://dx.doi.org/10.1016/j.matchemphys.2010.12.014.
[32] J.D. Robson, P.B. Prangnell, Dispersoid precipitation and process modelling in zirconium containing commercial aluminum alloys, Acta Mater. 49 (2001) 599–613, http://dx.doi.org/10.1016/S1359-6454(00)00351-7.
[33] N. Birbilis, R.G. Buchheit, Electrochemical characteristics of intermetallic phases in aluminum alloys an experimental survey and discussion, J. Electrochem. Soc. 152 (2005) B140–B151, http://dx.doi.org/10.1149/1.1869984.
[34] A. Steuwer, M. Dumont, J. Altenkirch, S. Birosca, A. Deschamps, P.B. Prangnell, P.J. Withers, A combined approach to microstructure mapping of an Al–Li AA2199 friction stir weld, Acta Mater. 59 (2011) 3002–3011, http://dx.doi.org/10.1016/j.actamat.2011.01.040.
[35] B. Decreus, A. Deschamps, F. De Geuser, P. Donnadieu, C. Sigli, M. Weyland, The influence of Cu/Li ratio on precipitation in Al–Cu–Li–x alloys, Acta Mater. 61 (2013) 2207–2218, http://dx.doi.org/10.1016/j.actamat.2012.12.041.
[36] A. Buis, J. Schijve, Stress corrosion cracking behavior of Al Li 2090-T83 in artificial seawater, Corrosion 48 (1992) 898–909, http://dx.doi.org/10.5006/1.3315891.
[37] Y. Ma, X. Zhou, W. Huang, G.E. Thompson, X. Zhang, C. Luo, Z. Sun, Localized corrosion in AA2099-T83 aluminum–lithium alloy: the role of intermetallic particles, Mater. Chem. Phys. 161 (2015) 201–210, http://dx.doi.org/10.1016/j.matchemphys.2015.05.037.
[38] A. Glenn, T. Muster, C. Luo, X. Zhou, Corrosion of AA2024-T3 part III: propagation, Corros. Sci. 53 (2011) 40–50, http://dx.doi.org/10.1016/j.corsci.2010.09.035.
[39] U. Donatus, G.E. Thompson, J.A. Omotoyinbo, K.K. Alaneme, S. Aribo, O.G. Agbabiaka, Corrosion pathways in aluminium alloys, Trans. Nonferrous Met. Soc. China 27 (2017) 55–62, http://dx.doi.org/10.1016/S1003-6326(17)60006-2.